Science Advances Manuscript Template

Front Matter

Title

A 18,000-year Record of Tropical Land Temperature, Convective Activity and Rainfall Seasonality from The Maritime Continent

Authors

Rienk H Smittenberg [1*], Kweku A Yamoah [1†], Frederik Schenk [1,2], Akkaneewut Chabangborn [1‡], Sakonvan Chawchai [1‡], Minna Väliranta [3], Barbara Wohlfarth [1*]

Affiliations

[1] Department of Geological Sciences and Bolin Centre for Climate Research, Stockholm University, Stockholm, Sweden.

[2] Rossby Centre, Swedish Meteorological and Hydrological Institute, 601 76 Norrköping, Sweden.

[3] Environmental Change Research Unit, Department of Environmental Sciences, University of Helsinki, Finland.

† now at School of Geography, University of Birmingham, Birmingham, UK.

‡ now at Department of Geology, Chulalongkorn University, Bangkok 10330, Thailand.

[*] Corresponding authors: rienk.smittenberg@geo.su.se; barbara.wohlfarth@geo.su.se

Abstract

The maritime continent exports an enormous amount of heat and moisture to the rest of the globe via deep atmospheric convection. How this export has changed through time during the last deglacial period and through the Holocene, is hardly known yet critical for the understanding of global climate dynamics. Here we present a continuous paleoclimate record from southern Thailand covering the last 18,000 years, including the first land-based temperature reconstruction of tropical SE Asia. We found evidence for a strongly seasonal climate for most of the deglacial period, causing biomass burning and suppression of rainforest growth, despite rising CO_2 levels and increasing mean humidity. Temperatures were *ca.* 5°C cooler than today during the last cold stadial periods, and *ca.* 2°C warmer between 7000-2000 yr ago. We also find that tropical wet-season insolation (WSI) is a primary driver of deep atmospheric convection, exerting a strong influence on global climate dynamics.

Teaser

A Deglacial-Holocene climate record from NE Sundaland indicates a strong influence of orbital forcing and CO_2 levels.

MAIN TEXT

Introduction

The maritime continent (MC) forms the central part of the Indo-Pacific Warm Pool (IPWP), defined as the equatorial region with sea surface temperatures (SST) above 28ºC. This region is also called the 'steam engine of the world'; it constitutes a critical component of the global climate system by providing large amounts of latent heat to the higher latitudes via deep atmospheric convection, particularly via the monsoon systems (1). The MC also forms a key node in the tropical Walker circulation above the Indian and Pacific Ocean, which is modulated by the El Niño-Southern Oscillation (ENSO) (2) and Indian Ocean Dipole (IOD) (3). Changes in rainfall in the MC have large consequences for both society and ecosystems, where drought-induced biomass burning and peat oxidation can induce rapid release of large amounts of carbon to the atmosphere e.g. (4). A major change in the MC over the last glacial-interglacial (G-I) transition was the inundation of formerly exposed Sundaland and the Sahul shelf north of Australia. It has long been recognized that the submergence of this vast tropical landmass must have had substantial consequences for global-scale climate dynamics (3,5-8). Palynological data from the former North Sunda and Molengraaff rivers and their deltaic deposits indicate that the region was covered with lowland rainforest that included sedges, reeds, bamboo, palms and ferns, suggesting fairly humid conditions throughout the last glacial maximum (LGM) around Borneo (9,10). In contrast, other proxy records from the region indicate drier conditions during the LGM (6,11). Highest ('driest') $\delta^{18}O$ values are recorded in a Borneo speleothem record at that time (12), and evidence exists for forest contraction and generally drier conditions in both peninsular Malaysia and Palawan during the LGM suggesting the existence of a savannah corridor (13-15). The somewhat conflicting proxy evidence can be explained by the expanse of former Sundaland, which is about the size of the Amazon basin. Another explanation may lie in rainfall seasonality, which can strongly impact proxy records of both vegetation and the recorded water isotope signal. A main problem is, however, that the spatial coverage of high-resolution paleoclimate records from the region remains scant, which is partially explained by the fact that much of Sundaland has disappeared under the waves. Insight into the spatial patterns and mechanisms of the, sometimes rapid, climatic changes that occurred during the G-I transition, as well as over the Holocene, is therefore still limited for this climatically important region. Here, we present a high-resolution, very well dated (Fig. S1) and continuous 18,000 year-long multi-proxy record from lake Nong Thale Prong (NTP, 8°17´N, 99°37´E) located in southern Thailand at the northwestern border of former Sundaland (Fig. 1). Lake NTP is a shallow (<7 m water depth), small (~210 m^2) karst lake at ~60 m above sea level (16). More details of the lake setting can be found in an earlier publication (17) that focused on the ecological evolution over the last 150 years using ancient DNA and lipid biomarkers. We used the stable carbon isotopic composition of leaf wax-derived long-chain *n*-alkanes ($\delta^{13}C_{wax}$) as a proxy for the relative abundance of C3 vs. C4 vegetation, which is influenced by pCO_2, temperature and seasonality (11,18). This data set was combined with the stable hydrogen isotope composition of the same leaf wax alkanes (δD_{wax}) and charcoal to gain further information about hydroclimate (19) and seasonality. We also present the first high-resolution land-based temperature record of the IPWP, based on bacterial-derived branched glycerol dialkyl glycerol tetraethers (brGDGTs) (20-22). The combined proxy records reveal how the aerial exposure and subsequent inundation of Sundaland interacted with orbital variation and other climate forcings to impact the hydroclimate of SE Asia.

Results

Proxy validation

We performed a present-day proxy evaluation and calibration by comparing proxy data analyzed from the surface sediments with instrumental data for the last century. δD_{wax} (17) closely follows the annual precipitation amount (Fig. 2a), where a 10‰ decrease in δD_{wax} corresponds to a 25% reduction in rainfall. This confirms earlier work relating convective activity with both greater rainfall and isotopic fractionation (the 'amount effect', e.g. (23) assuming that δD_{wax} predominantly reflects δD_{precip} after biosynthetic fractionation. Previous research has shown that the hydrogen isotopic composition of both terrestrial and aquatic biomarkers generally reflects that of their source water, although with an offset primarily due to biosynthetic fractionation effects (19,24,25). In the humid tropics, the fractionation ($\varepsilon_{wax/water}$) was found to be fairly constant at 130‰ (26). Using this fractionation factor, back-calculated δD values for precipitation of the last century ranges between -40‰ and -60‰, reflecting actual measurements for the region (27).

Reconstructed mean annual air temperatures ($MAAT_{RC}$) (Fig. 2b) obtained using the relative abundance of microbial-derived branched GDGTs (21,22), were recalibrated using instrumental temperature data, thus generating a local calibration for this molecular proxy. $MAAT_{RC}$ and δD_{wax} correlate strongly with each other (Fig. 2c), and have the same relation to each other as observed during the seasonal cycle: clear skies during the drier seasons and years with less convective rainfall allow for higher surface temperatures, whereas high clouds associated with deep convection result in a cooling of the surface due to reflection and atmospheric absorption of shortwave radiation (28), an effect that is particularly strong in monsoonal Asia (29).

Sedimentology and limnology

The 18,000 year-long lake NTP sequence consist of organic rich gyttja with TOC contents ranging between 10-40% (Fig. S2). TOC contents vary stepwise between 10 and 40% during the deglacial part of the core, high TOC contents between 9.5 - 4.2 ka BP, turning to somewhat lower and more variable contents over the last few millennia. Besides some variation caused by changes in minerogenic input, we interpret the TOC changes as mainly caused by alternations between meromictic conditions with permanent bottom water anoxia - leading to preservation of organic matter, and monomictic conditions - resulting in greater organic matter oxidation within the sediments. Stratification in tropical lakes is sensitive to small changes in the lake water level between wet and dry seasons, heat budgets and climate (e.g., wind stress), and other limnological or even ecological feedbacks (30). Given this multitude of factors, we do not attempt to interpret the TOC content. Notably, there is no correlation between the variable TOC content and the lipid biomarker proxies presented further below. This indicates that lake stratification and preservation of organic matter did not influence the primary climatic signal of our proxy records.

The continuous occurrence of seeds of the aquatic plant taxon *Najas* (Fig. 3f; SI Table 4, Fig. S2) and a robust age model indicates that the shallow lake never dried out. *Cyperaceae* spp. remains, mostly seeds, also occur continuously throughout the sequence, except for the last few millennia when they are nearly absent.

The lower part of the sequence, deposited during Heinrich Stadial 1 (HS1, 18 - 14.7 ka BP), contains unidentified terrestrial plant remains including woody material, often co-occurring with charred plant remains and macroscopic charcoal; this was also the case for the Younger Dryas period (YD 12.8 - 11.5 ka BP). Charcoal was most abundant during HS1, then declined towards the end of the deglacial period, with irregular occurrences until the early Holocene around 9 ka BP. Ostracod shells are abundant throughout the HS1, leading to high carbonate contents, and this declines during the Bølling (Bø 14.7 - 14.0 ka).

Temperature reconstruction

$MAAT_{RC}$ (Fig. 3b) stays around 23-24°C during HS1, a 5°C cooling compared to the present. This is lower than the most recent estimate for the tropical ocean during the LGM (−4.2 to −3.7°C; (31) but is in line with estimates based on tropical glacier snow line elevations (32). Temperatures rose during the Bø to reach a maximum of 26°C soon after the Older Dryas event (OD 14.0 - 13.8 ka BP), but declined during the Allerød (Al, 13.8 - 12.8 ka BP) and again reached stadial values at the end of the YD. With the start of the Holocene temperatures rose steadily to reach 28-29°C between 7-2 ka BP. The last two millennia are characterized by a cooling trend to a present-day $MAAT_{RC}$ of around 27°C.

$\delta^{13}C_{wax}$ as combined proxy for pCO_2, temperature and rainfall seasonality

Stable carbon isotope ($\delta^{13}C$) values of both of the long-chain *n*-alkanes ($\delta^{13}C_{wax}$) (Fig. 3c) and the bulk (Fig. S2) reflects a change from a landscape dominated by C4 grasses and sedges at the beginning of the record, to a humid tropical ecosystem dominated by ^{13}C-

depleted C3 vegetation – likely forest - during the Holocene (*cf.* 33). The $\delta^{13}C$ record broadly follows the evolution of atmospheric CO_2 (Fig. 3d). This lends support to the hypothesis that low CO_2 concentration favored C4 vegetation during the LGM (18,34,35). Our observation compares well to tropical African records (36-38). Increasing fractionation against ^{13}C at higher pCO_2 levels and greater humidity (39,40) – regardless of plant type, can explain part of the trend. An exception to the general trend of increasingly more negative $\delta^{13}C$ from the LGM through the Holocene is a large excursion that starts at 16.0 ka BP, reaching the lowest $\delta^{13}C$ values at 13.8 ka BP.

δD_{wax} as proxy for precipitation

To further investigate past precipitation changes, we analyzed δD_{wax}, with higher resolution between 17-10 ka BP, to discern trends during deglaciation (Fig. 3a). δD_{wax} was corrected for the effect of global ice volume (41). A confounding factor in the interpretation of δD_{wax} is the potential effect of changing vegetation and associated change in fractionation (42). For instance, C3 and C4 plant types tend to fractionate differently against deuterium and may moreover respond differently to drought in order to minimize water loss while still allowing gas exchange through the stomata (33,43). The generally stronger biosynthetic fractionation against deuterium of C3 plants compared to C4 would however lead to an opposite behavior of δD_{wax} as observed: the increase in C4 during the Bølling period is associated with more negative δD_{wax}, not more positive. The same argument can be made from a possible transition from a grassy to more woody vegetation during the G-I transition, which would be expected to lead to less negative δD_{wax} values (42), but again the opposite is observed. From the perspective of vegetation change, our δD_{wax} record might thus even underestimate the original variations in source water δD.

Discussion

Deglacial climate evolution

The unusual $\delta^{13}C$ excursion that starts at 16.0 ka BP suggests a renewed contribution of C4 vegetation to the carbon pool in this interval, even though the excursion is coincident with continued warming and its onset correlates with a change in the rate of increase in atmospheric pCO_2 (Fig. 3). The behavior of the $\delta^{13}C$ record indicates that the tropical lowland ecosystem of Sundaland represented an ecotone inhabiting the C3/C4 crossover line during the deglacial period. This ecosystem was sensitive to the antagonistic effects of rising pCO_2 and rising temperature on C3 versus C4 plants, where higher temperatures and/or lower pCO_2 favor C4 plants. However, a third important climatic factor also favors non-perennial C4 vegetation: rainfall seasonality (11). Seasonal dryness was likely promoted by the presence of Sundaland, which only became fully inundated around 11 ka BP during Meltwater Pulse 1b (44). This large landmass prevented the dry northern winds of the Asian winter monsoon from picking up moisture over the Sunda Sea as they do today. This effect was probably promoted by orbital forcing: insolation during NH winter declined while summer insolation increased over the deglacial period, favoring the strength of both the winter and summer monsoon. Strong seasonality promotes biomass production during the wet season, which then serves as fuel for biomass burning during a longer dry season (45). This severely limits the establishment of perennial C3 forests that would otherwise outcompete non-perennial C4 vegetation as atmospheric CO_2

levels rose. The charcoal record (Fig. 3f, SI Table 4) provides evidence that fires were a persistent feature during the entire deglacial period, especially during HS1. We therefore conclude that the return towards a larger contribution of C4 vegetation after 16 ka BP arose from a combination of both rising temperatures and greater seasonality in rainfall patterns, temporarily offsetting the C3-promoting effect of increasing pCO_2. The return of C3 vegetation after 13.8 ka BP indicates that the region started to have year-round precipitation, reducing seasonal drying and fire. The general trend in $\delta^{13}C$ observed at NTP also is evident in the lower resolution IPWP record from Lake Towuti on Sulawesi (46) (Fig. S3), supporting the interpretation of the combined influence of pCO_2 and rainfall seasonality over the entire IPWP over glacial-interglacial timescales.

Starting at 18 ka BP, the δD_{wax} record increases to reach highest (least negative) values around 16 ka BP (Fig. 3), indicating that the driest conditions with the weakest convection and greatest evapotranspiration (47) occurred during HS1, culminating at Heinrich Event 1. This is followed by a rapid decrease during the Bø, and, similar to the $MAAT_{RC}$ and $\delta^{13}C$ records, and subsequent a sharp reversal at the start of the Al. δD_{wax}, $MAAT_{RC}$ and $\delta^{13}C$ track each other until the YD, with lower (higher) δD_{wax} and higher (lower) $MAAT_{RC}$ - suggesting warmer and wetter (colder and drier) conditions – consistent with inferences from the $\delta^{13}C$ record of patterns of change in C4 vegetation. The combined records suggest that the period of high rainfall seasonality also had wetter wet seasons. Yet, despite increased humidity and warmer conditions during the wet season, C4 grasses and sedges were not completely replaced by C3 plants.

We suggest that the rapid decrease in δD_{wax} between 16 and 14 ka BP was driven by an increase in the convective strength over Sundaland with rising temperatures during the Bø. Large-scale convective activity and rainfall amount are the dominant factors that influence water isotope values in tropical SE Asia, in addition to changes in moisture source region (27). Today, during NH summer (JJA), most moisture in southern Thailand is derived from the Indian Ocean, but during the wettest autumn season (SON) there is also a contribution from the South China Sea. In the past, however, moisture derived from evapotranspiration over Sundaland likely also contributed to the isotopic signature. Moreover, longer air mass trajectories over land would have caused a larger rainout effect, leading to lower water isotope values similar to those of present-day mainland SE Asia (27). The lower values might have been exacerbated by the seasonality of rainfall, because the final isotopic signal of water available for plant growth is biased towards that of the wet season (with lowest δD_{precip}) because of its larger contribution to the weighted annual mean.

The rapid sea level rise during MWP1a changed the hydrologic gradient and reduced the flow of Sundaland river systems. Together with monsoon intensification this most likely transformed the entire Sundaland region into a vast expanse of tropical wetlands (1) with abundant moisture and isotope recycling comparable to the present-day Amazon basin. The parallel reversal of δD_{wax}, $\delta^{13}C$ and $MAAT_{RC}$ around 13.8 ka BP, coincident with the OD event (Fig. 3), indicates a system change towards decreasing rainfall seasonality and a more marine climate. Higher year-round moisture availability would result in a greater contribution of less-depleted δD_{prec} during the cooler winter monsoon months, thereby raising annual mean δD. The lowering of MAAT can be explained by greater evaporative cooling, i.e. more energy is taken up by latent heat, to the expense of sensible heat. It is also possible that the cold winter monsoon had already started to strengthen during the Al period in response to a southward movement of the mean position of the intertropical convergence zone (ITCZ) caused by NH cooling, something that continued until the end of the YD (~11.5 ka BP). The hypothesis of a southward ITCZ is supported by the coherent patterns in the variability of δD_{wax} during the YD and the Greenland ice core $\delta^{18}O$ record, with shifts in the mean position of the ITCZ in response to latitudinal temperature gradients (48). After the YD, however, δD_{wax} continues to increase until 11 ka BP, in opposition to the rapid change in the Greenland record, but interestingly enough also opposite to the local $MAAT_{RC}$. We attribute this to the development of an even more equable hydroclimate throughout the year, with an increased relative influence of 'dry'-season rainfall with higher δD values, sourced from the Gulf of Thailand and the South China Sea.

Orbital forcing of Holocene and deglacial climate, and seasonality effects

After 11 kyr BP, δD_{wax} and $MAAT_{RC}$ vary again in tandem. Both show a generally asymptotic trend towards the warmest and wettest conditions peaking at ~4.5 ka BP. This indicates that the 'steam engine of the world', the IPWP, was at full power during the mid-Holocene thermal maximum, exporting greatest amounts of latent heat, i.e. moisture, to the Northern Hemisphere during this time. This long-term coupling between δD and $MAAT_{RC}$ at orbital to millennial scales is opposite to that of higher frequency relationships at annual to decadal scales (Fig. 2), where the total insolation is distributed between latent and sensible heat. Orbital-scale changes in the seasonal distribution of insolation apparently steer $MAAT_{RC}$ and convective strength in the same direction. The precessional cycle has indeed long been identified as the dominant component of orbital forcing influencing tropical and monsoonal climate (29,49). NH summer insolation (JJA) is most commonly used to explain the waxing and waning of monsoon strength, even though leads and lags between proxy records exist. In the tropics, however, the season of most intense rainfall does not occur during JJA. Thus, we compare our records with 'wet season' insolation (WSI), i.e., the mean monthly insolation during the wettest part of the annual cycle at 8ºN. Indeed, δD_{wax} follows the insolation curve for the wettest months, September-November (Fig. 4) (50), although with a notable excursion during the Bø/Al-YD periods, which we attribute to the influence of Sundaland and strong seasonality, as discussed above.

The 7% variation of WSI over the last 18,000 years (418 - 446 kW/m^2) (50) thus appears to be a main driver of both surface (temperature) and atmospheric (latent, convective) heat flux. This observation is consistent with a Borneo (4ºN) speleothem record (51), where $\delta^{18}O$ is correlated with the wettest months at that latitude (Fig. 4). The δD_{wax} record from Lake Towuti (Sulawesi) has been interpreted as being driven primarily by changes in moisture source and air trajectories (52), but it also shows a strong correspondence with WSI at 2ºS (Dec&Jan, during the passing of the ITCZ) (Fig. 4). Both δD_{wax} records (NTP and Towuti) show a sensitivity to WSI of -1.4‰ per W/m^2, as does the Borneo record when scaled by a factor of eight for $\delta^{18}O$ according to the global meteoric water line. Combined, these records provide further evidence for the influence of the precessional cycle on the isotopic composition of regional precipitation, via the combined mechanisms of regional convective activity and associated amount of precipitation. This is exacerbated by secondary effects of seasonality, which also affects the distribution between latent and sensible heat. In the tropics there is a clear correlation between insolation and rainfall amount (Fig. S10), with at present lowest values in June and July (Fig. S9) (53). Over the course of a precessional cycle, the shift in seasonal distribution of solar energy can be as much as 15%, which must be causing a large effect on seasonality. At and near the equator, the 'dry' season may even have shifted from NH summer to SH summer (Fig. S9), and the wettest season more towards or away from the March and September annual maximums, depending on the orbital phase. Because of this we did not assign a wet season insolation curve to the Tangga Cave record at Sumatra (Fig. 4).

At our site lake Nong Thale Prong at 8°N, the present-day annual insolation curve exhibits two highs: one in April and one in August/September (Fig. S5), when the sun's altitude is 90° at noon. The annual movement of the ITCZ and the Monsoon system behaves in an attenuated fashion (Fig. S6). From January onwards, temperatures rise (Fig. S7) but precipitation remains low until May, because the ITCZ remains south. Dry conditions with low cloud cover cause low albedo, resulting in highest surface temperatures in April (Fig. S7). The ITCZ passes over quickly going northwards during May and June, to merge with the Asian Summer Monsoon system during the NH summer (Fig. S6). The Monsoon/ITCZ moves back towards the equator in NH autumn, causing the strongest period of convective precipitation over the northern IPWP from September-November (Figs. S6 and S7). During this time, much of the incoming radiation is reflected by high convective clouds, or is used to generate latent heat, leading to reduced surface temperatures (Fig. S7).

Between 6-4 ka BP, perihelium (the moment the earth is closest to the sun during its elliptical orbit) occurred in September-October, causing 5% greater insolation in September compared to today (Fig. S5). This stronger WSI for the SE Asian Monsoon, and the northern IPWP, will have caused warmer ocean surfaces and subsequently greater evaporation and convective activity both in the northern Indian Ocean (specifically the Bay of Bengal), as well as the South China sea. All this explains that lowest δD_{wax} values are observed in the mid Holocene. On top of that, NH springtime precipitation was likely lower because of lower insolation levels (Figs. S6 and S8), causing a stronger bias of autumn rainfall towards the annual mean.

Higher mid-Holocene MAATs result from a combination of drier and sunnier spring months, compensating for relatively low insolation levels (more sensible heat, less latent heat), and cloudy wet months that however receive highest solar inputs. Our data are thus consistent with the theory that the precessional cycle caused greater seasonality in the mid Holocene, compared to the low seasonality period we currently experience.

Looking further back, the seasonal pattern of insolation at 20 ka BP is similar as today (Fig. S7), but over the ensuing deglacial period (e.g. towards 14 ka BP) perihelion shifts towards NH spring. Being a mirror case of the situation at 6 ka BP, this would cause higher convective activity in the northern IPWP during NH spring with moisture sourced from the Pacific side. In NH autumn, the lower insolation would have caused a weakened ITCZ convection. Different to today, however, was the presence of Sundaland. Air masses coming from the northeast would not have been able to pick up as much moisture as they can today over the South China Sea. Consequently, the greater NH spring insolation only could lead to more rainfall when Sundaland became a large wetland, allowing more land surface evapotranspiration. Until then, the annual total rainfall would have derived almost exclusively from the autumn. After 14 ka BP, the perihelion moves towards NH summer, and insolation remains high from spring through summer and into the autumn. After 12 ka BP, insolation becomes ever more focused on the autumn (all autumn months go 'up', see Fig. S8), until 6 ka BP, thus aligning ever more with the annual movement of the ITCZ and the period of strongest convection. Over the last millenniums, perihelium has shifted from NH winter towards spring.

The relative strength of insolation and related convective activity distributed over the year will have had its effect on the annual weighted mean of δD of precipitation. Results for nearby Phuket (27) indicate only a relatively small range in $\delta^{18}O$ through the year, from -2‰ (i.e. δD = -7‰) in April to -8‰ (δD = -55‰) in November, with an annual weighted average of -5.5‰ (δD = -35‰). The moment a shorter season is responsible for the majority of the annual sum, i.e., when the perihelion aligns with the wettest months in autumn, then the weighted mean annual isotope value will shift towards that season. This is the likely situation in the mid Holocene around 6 ka BP where isotopically relatively heavy spring precipitation will have contributed less, however the stronger convective activity during the wet autumn season will likely have caused more depleted wet season precipitation as well. Together this causes a bias towards lower mean annual δD values at times of strong seasonality. This seasonal bias also means that there does not need to be any close relation between total annual rainfall and the mean isotopic composition. The seasonal bias on the mean annual isotopic composition can explain many isotope records from the tropics, without a large need to infer changes in rainfall amount, or changes in moisture source.

Lastly, we briefly comment on the effect of the precessional cycle on advected moisture. In the early Holocene, perihelion (i.e., highest insolation) occurred during the start of the Asian summer monsoon, when the advected moisture in mainland SE Asia does not yet reach very depleted values ($\delta^{18}O$ = -18‰ (27)). In the mid-late Holocene, however, perihelion has shifted to the autumn, at a time when the moisture reaching mainland SE Asia is already much more depleted. The expected shift of the Monsoon strength towards the autumn will thus also cause a shift in the mean isotope composition - even if at the local scale insolation and therefore total monsoon strength has already decreased. The end result is an attenuation of 'peak isotope', because of the source effect, and not because of the amount effect. This effect can explain the temporal shift of 'peak isotope' away from the time perihelium occurred during classical NH summer (JJA, between 10-8 ka BP) towards later (8-6 ka BP) as observed in the Chinese speleothem records.

Influence of IPWP hydroclimate on the Asian monsoon and ENSO

The trends in the NTP δD_{wax} record are similar to those in the Asian speleothem $\delta^{18}O$ records (54,55) (Fig. 5), including the OD event and the 'peak isotope' feature at the beginning of the Al. NTP δD_{wax} also tracks the Greenland ice core record (Fig. 5), reflecting the impact of high-latitude NH forcing on tropical climate. NTP receives most of its moisture from the Indian Ocean, in contrast to the East Asian speleothems, which also receive significant summer monsoon moisture from the East (27,55). The shared patterns of variation are consistent with modeling studies (56,57), which have shown that East Asian speleothem $\delta^{18}O$ records reflect the isotopic composition of the advected moisture, as much or more so than rainfall amount, and that large-scale convection patterns are the main drivers of the isotopic composition of precipitation (27). Our results, which are similar to those from a recent study in northern Thailand (8), demonstrate that the exposure and inundation of Sundaland played a decisive role in affecting the water isotopic composition not across mainland East Asia, but also in Thailand. The same factors that lowered δD_{wax} at our site (more rainout and more land-derived moisture from Sundaland, and greater seasonality), must also have applied further inland. Remote processes upstream of the SE Asian Monsoon, such as the presence / inundation of Sundaland, as well as precession-forced changes in WSI in the lower tropics, need to be considered when interpretating SE Asian water isotope records in sediments and speleothems. Experiments with isotope-enabled general circulation models are needed to gain further insight.

Another notable feature of the δD_{wax} record are the positive ('dry') excursions between 4 and 3 ka BP, which is coincident with the onset of the Meghalayan age (Fig. 3), characterized by megadroughts observed in multiple regions (58). The dry events occur on top of a general decline in convective activity, which follows the decrease in WSI after 5 ka BP. Our results of a wettest and warmest mid Holocene extend the recent finding (59) of a warmer mid Holocene thermocline in the IPWP east of 115°E, caused by greater September insolation. The warmer and deeper thermocline causes a stronger zonal thermal difference across the equatorial Pacific, which further promotes deep atmospheric convection and rainfall over western equatorial Pacific in a positive feedback mechanism, inducing a stronger Walker circulation and suppression of ENSO activity. The interaction of the precessional and seasonal cycles that act upon the IPWP, being the 'steam engine of the world', thus appears to play a decisive role in global climate dynamics by regulating the amount of latent heat exported to the higher latitudes. In this respect, we even speculate that the inundation and warming of Sundaland and may have provided a key positive feedback mechanism during the last G-I transition, and possibly also earlier ones.

Materials and Methods

Sampling and sample processing

Two parallel sediment cores were retrieved in one-meter sections using a rod-operated Russian corer from a small raft at the deepest part of the lake. After recovery, the sections were wrapped in foil and secured and transported in PVC tubes to Stockholm University, where they were stored at 4°C until further analysis. Sub-samples were taken in contiguous 1-cm increments and split to accommodate subsequent analyses. One half of the samples was utilized for macrofossil and charcoal analysis and radiocarbon dating. The other half of the samples was freeze-dried and analysed for loss-on-ignition (LOI), bulk total organic carbon (TOC), nitrogen (TN) and their isotopes, lipid biomarkers and compound-specific hydrogen and carbon isotopes. For LOI, samples were dried overnight at 105°C, ground and then combusted at 550 °C for 3h. LOI was calculated as a percentage of the dry sample weight to obtain an estimate of the organic matter and carbonate content. In parallel, a sediment-water interface surface core covering the last 150 years was retrieved and sampled on site in one cm slices (17).

Macrofossil analysis and radiocarbon dating

Approximately 380 samples were sieved under running water (mesh sizes 0.5 and 0.25 mm) to recover plant macrofossils for radiocarbon dating. Plant remains were picked with tweezers under a binocular microscope, described, and rinsed multiple times in deionized water, placed in pre-cleaned glass vials and dried overnight at 105 °C. 59 samples were dated at the 14Chrono Centre, Queen's University Belfast, where pre-treatment and measurement followed the methodology described in (60). Based on these, an age-model (SI Fig. 1) was constructed using Bacon, a Bayesian statistics-based routine (61) that estimates the accumulation rate for sediment segments based on the radiocarbon dates calibrated using the intCal13 NH calibration curve (62).

Bulk geochemistry

%TOC, %TN and bulk $\delta^{13}C_{org}$ and bulk $\delta^{15}N_{bulk}$ were measured on a Carlo Erba NC2500 elemental analyser, coupled to a Finnigan MAT Delta^{+} mass spectrometer. To remove carbonates, samples were fumigated with HCl within a dessicator prior to analysis. $\delta^{13}C_{bulk}$ is expressed in ‰ against the Vienna PeeDee Belemnite (VPDB) standard, and had an analytical error of less than ±0.15‰. $\delta^{15}N_{bulk}$ are reported in ‰ relative to air (N), with an analytical error of ±0.15‰.

Lipid biomarkers

Lipid extraction was performed on freeze-dried samples by sonication with a mixture of dichloromethane and methanol (DCM-MeOH 9:1 v/v) for 20 minutes and subsequent centrifugation. The process was repeated three times and supernatants were combined. Aliphatic hydrocarbon fractions were isolated from the total lipid extract using silica gel columns (5% deactivated) that were first eluted with pure hexane (F1) and subsequently with a mixture of DCM-MeOH (1:1 v/v) to obtain a polar fraction (F2). A saturated hydrocarbon fraction was obtained by eluting the F1 fraction through 10% $AgNO_3$ impregnated silica gel using pure hexane as eluent. The saturated hydrocarbon fractions were analyzed by gas chromatography – mass spectrometry for identification and quantification, using a Shimadzu GCMS-QP2010 Ultra. C_{21} to C_{33} *n*-alkanes were identified based on mass spectra from the literature and retention times. The concentrations of individual compounds were determined using a calibration curve made using mixtures of C_{21}-C_{40} alkanes of known concentration.

Leaf wax hydrogen and carbon isotope analysis

The hydrogen isotopic composition of *n*-alkanes (expressed in delta notation in ‰ against VSMOW) was analyzed by gas chromatography–isotope ratio monitoring–mass spectrometry (GC-IRMS) using a Thermo Finnigan Delta V mass spectrometer interfaced with a Thermo Trace GC 2000 using the HTC reactor of a GC Isolink II and Conflo IV system. Helium was used as a carrier gas at constant flow mode and the compounds separated on a Zebron ZB-5HT Inferno GC column (30 m x 0.25 mm x 0.25µm). A standard set of alkanes with known isotopic composition (obtained from A. Schimmelmann, Indiana University, USA) was used for daily calibration of the reference gas. The average standard deviation of δD values was 5‰. The reported δD_{wax} values are the average of the most abundant long chain *n*-alkanes: C_{27}, C_{29} and C_{31}. To correct for the higher global average of global oceanic δD during lower sea levels, the δD values of the *n*-alkanes were ice volume corrected (*c.f.* (41) as follows: $\delta D_{wax\text{-}c} = (\delta D_{wax} + 1000) / (\delta O^{18}_{w} * 8 * 0.001 + 1) - 1000$, with interpolated ocean water δO^{18}_{w} values (63).

$\delta^{13}C_{wax}$ was measured on the same compounds on the same system and the same isotope standards, except for the use of the combustion reactor. $\delta^{13}C_{wax}$ values are the average of C_{27}, C_{29} and C_{31} alkanes, expressed in delta notation in ‰ against VPDB, with an average standard deviation of 0.5‰.

Glycerol dialkyl glycerol tetraether (GDGT) analysis and temperature reconstruction

Branched glycerol dialkyl glycerol tetraethers (brGDGTs) were measured on the F2 fractions after reconstituting in MeOH:DCM 9:1 and subsequent filtration through 0.45 µm PTFE filters, following published protocols (64). Analysis was done using a Thermo-Dionex HPLC connected to a Thermo Scientific TSQ quantum access triple quadrupole mass spectrometer, using an APCI interface. Chromatographic separation was achieved on a Kinetex C18-XB reverse phase column using a gradient of mobile phase A: MeOH with 0.04% formic acid and mobile phase B: propan-2-ol with 0.04% formic acid. GDGTs were detected in SIM mode at *m/z* 1020 (scan width 7, 0.2s), 1034 (width 7, 0.2s), 1048 (width 7, 0.2s), 1296 (width 17.5, 0.5s). Quantification was performed using Excalibur software, using the (M+) and (M+1) ions of the GDGTs. More details can be found elsewhere (64). MBT and CBT proxies were calculated following (65).

A basic prerequisite for the valid use of brGDGTs is a relatively high branched-over-isoprenoid tetraether (BIT) index, which was 1.0 throughout the core. Reconstructed pH values, based on the CBT index (65) were 8.0±0.2 over the entire core, with lowest values during the YD and a downward trend for the last 2000 years (Fig. S4). This means that temperature is the dominant environmental factor exerted on the brGDGT distribution. At the time of measurement, we had not adopted the new HILIC-based method which separates between 5-methyl and 6-methyl branched GDGTs (66) but used our own method based on reverse phase chromatography (64), similar to the one used by (67), and which compared well with the original method using a cyano column. As a consequence, we do not have individual quantifications of 5-methyl and 6-methyl branched GDGT isomers used in the revised MBT'_{5me} temperature proxy for mineral soils (68), peats (69), or East African lakes (20). However, for high temperatures as is the case for our site, the main response to temperature is a shift between tetra- and pentamethylated GDGTs, which makes the differentiation between 5- and 6-methyl GDGTs less relevant than in cold environments. The relative abundance of tetra-, penta- and hexamethylated GDGTs plot in the same region as datasets produced with the HILIC method from east African lakes and from global soils and peats (Fig S4). This strengthens the confidence that the brGDGTs we measured can be used as a temperature proxy. Among the various GDGT-temperature calibrations that have been developed since the original one (65), we chose to apply the global lake calibration of (22) for lakes with pH<8.5, which also included data from nearby lake Towuti:

$$MAAT_{Sun\text{-}cal} = 3.949 + 38.213\ MBT - 5.593\ CBT \qquad \text{(Eq. 1)}$$

The MBT/CBT-based MAAT (°C) reconstruction using the global regression model (22) shows a good agreement with temperature observations in the region (closest grid point at 8.25° N; 99.25° E from the University of East Anglia Climate Research Unit dataset CRU TS3.23) (70) for the overlapping period of 1903-2001. There is however an offset and overestimation of variability in the proxy reconstruction using the global lake calibration relative to the local temperature. To adjust the reconstruction to our local conditions, we re-calibrated the global reconstruction by replacing the mean of the $MAAT_{Sun\text{-}cal}$ values obtained using the global regression ($\mu_{proxy\text{-}global}$) and standard deviation ($\sigma_{proxy\text{-}global}$) with those of local conditions from CRU TS3.23. This was done by first normalizing the proxy record for the overlapping period 1903-2001 and then re-normalize it using the mean ($\mu_{obs\text{-}local}$) and standard deviation ($\sigma_{obs\text{-}local}$) of the local observations for the same time period (Eq. 2).

$$MAAT_{i,local} = \left[(x_{i,proxy-global} - \mu_{Proxy-global})\frac{\sigma_{Obs-local}}{\sigma_{Proxy-global}}\right] + \mu_{Obs-local} \qquad \text{(Eq. 2)}$$

resulting in a record of recalibrated $MAAT_{RC}$ values. This re-calibration effectively adjusts the intercept and slope of the original calibration so that the proxy data reflects the mean and annual variability observed over the instrumental record. Generating a new calibration by regression of the GDGT data with the instrumental record is not straightforward, because the samples do not correspond to annual measurements but approximately 3 years, with an error of the age estimate based on ^{210}Pb dating that increases with depth.

We even performed the same exercise using the original calibration (65), and came to the same results (Fig. S4a). It is important to note that all data come from one location where the microbial ecology of the brGDGT-producing organisms and the dominant environmental factors vary much less compared to the globally distributed surface sediment datasets used to generate the GDGT calibrations. For reference, the RMSE of the East African lake calibration (20) is approximately 2.5°C.

References

1. P. De Deckker, The Indo-Pacific Warm Pool: critical to world oceanography and world climate. *Geoscience Letters* **3**, 20 (2016).

2. A. Timmermann, *et al.*, El Niño–Southern Oscillation complexity. *Nature* **559**, 535–545 (2018).

3. M. Mohtadi, M. Prange, E. Schefuß, T. C. Jennerjahn, Late Holocene slowdown of the Indian Ocean Walker circulation. *Nat Commun* **8**, 1–8 (2017).

4. J. T. Randerson, *et al.*, Fire emissions from C3 and C4 vegetation and their influence on interannual variability of atmospheric CO2 and δ13CO2. *Global Biogeochemical Cycles* **19** (2005).

5. A. Koutavas, S. Joanides, El Niño-Southern Oscillation extrema in the Holocene and Last Glacial Maximum: ENSO EXTREMA IN THE HOLOCENE AND LGM. *Paleoceanography* **27** (2012).

6. P. N. DiNezio, J. E. Tierney, The effect of sea level on glacial Indo-Pacific climate. *Nature Geosci* **6**, 485–491 (2013).

7. P. N. Di Nezio, *et al.*, The climate response of the Indo-Pacific warm pool to glacial sea level. *Paleoceanography* **31**, 866–894 (2016).

8. K. A. Yamoah, *et al.*, A muted El Niño-like condition during late MIS 3. *Quaternary Science Reviews* **254**, 106782 (2021).

9. X. Wang, X. Sun, P. Wang, K. Stattegger, Vegetation on the Sunda Shelf, South China Sea, during the Last Glacial Maximum. *Palaeogeography, Palaeoclimatology, Palaeoecology* **278**, 88–97 (2009).

10. L. X. Sun Xiang Jun, L. X. Sun Xiang Jun, Vegetation and Climate on the Sunda Shelf of the South China Sea During the Last Glactiation-Pollen Results from Station 17962. *J Integr Plant Biol* **44** (2002).

11. N. Dubois, *et al.*, Indonesian vegetation response to changes in rainfall seasonality over the past 25,000 years. *Nature Geoscience* **7**, 513–517 (2014).

12. J. W. Partin, K. M. Cobb, J. F. Adkins, B. Clark, D. P. Fernandez, Millennial-scale trends in west Pacific warm pool hydrology since the Last Glacial Maximum. *Nature* **449**, 452–455 (2007).

13. C. M. Wurster, H. Rifai, B. Zhou, J. Haig, M. I. Bird, Savanna in equatorial Borneo during the late Pleistocene. *Sci Rep* **9**, 1–7 (2019).

14. L. R. Heaney, A synopsis of climatic and vegetational change in Southeast Asia. *Climatic Change* **19**, 53–61 (1991).

15. C. M. Wurster, *et al.*, Forest contraction in north equatorial Southeast Asia during the Last Glacial Period. *Proceedings of the National Academy of Sciences* **107**, 15508–15511 (2010).

16. S Snansieng, Gitisan, N, P. Sripongnan, Geological map of Changwat Nakhon Si Thammarat. (1976).

17. K. A. Yamoah, *et al.*, A 150-year record of phytoplankton community succession controlled by hydroclimatic variability in a tropical lake. *Biogeosciences* **13**, 3971–3980 (2016).

18. H. Pinto, R. E. Sharwood, D. T. Tissue, O. Ghannoum, Photosynthesis of C3, C3–C4, and C4 grasses at glacial CO2. *J Exp Bot* **65**, 3669–3681 (2014).

19. D. Sachse, *et al.*, Molecular Paleohydrology: Interpreting the Hydrogen-Isotopic Composition of Lipid Biomarkers from Photosynthesizing Organisms. *Annu. Rev. Earth Planet. Sci.* **40**, 221–249 (2012).

20. J. M. Russell, E. C. Hopmans, S. E. Loomis, J. Liang, J. S. S. Damsté, Distributions of 5-and 6-methyl branched glycerol dialkyl glycerol tetraethers (brGDGTs) in East African lake sediment: Effects of temperature, pH, and new lacustrine paleotemperature calibrations. *Organic Geochemistry* **117**, 56–69 (2018).

21. S. Schouten, E. C. Hopmans, J. S. Sinninghe Damsté, The organic geochemistry of glycerol dialkyl glycerol tetraether lipids: A review. *Organic Geochemistry* **54**, 19–61 (2013).

22. Q. Sun, *et al.*, Distributions and temperature dependence of branched glycerol dialkyl glycerol tetraethers in recent lacustrine sediments from China and Nepal. *Journal of Geophysical Research: Biogeosciences* **116** (2011).

23. S. Bony, C. Risi, F. Vimeux, Influence of convective processes on the isotopic composition (δ^{18}O and δD) of precipitation and water vapor in the tropics: 1. Radiative-convective equilibrium and Tropical Ocean–Global Atmosphere–Coupled Ocean-Atmosphere Response Experiment (TOGA-COARE) simulations. *J. Geophys. Res.* **113**, D19305 (2008).

24. D. Sachse, J. Radke, G. Gleixner, Hydrogen isotope ratios of recent lacustrine sedimentary n-alkanes record modern climate variability. *Geochimica et Cosmochimica Acta* **68**, 4877–4889 (2004).

25. A. L. Sessions, T. W. Burgoyne, A. Schimmelmann, J. M. Hayes, Fractionation of hydrogen isotopes in lipid biosynthesis. *Organic Geochemistry* **30**, 1193–1200 (1999).

26. S. J. Feakins, *et al.*, Plant leaf wax biomarkers capture gradients in hydrogen isotopes of precipitation from the Andes and Amazon. *Geochimica et Cosmochimica Acta* **182**, 155–172 (2016).

27. Z. Wei, *et al.*, Influences of large-scale convection and moisture source on monthly precipitation isotope ratios observed in Thailand, Southeast Asia. *Earth and Planetary Science Letters* **488**, 181–192 (2018).

28. A. H. Sobel, E. D. Maloney, G. Bellon, D. M. Frierson, Surface fluxes and tropical intraseasonal variability: A reassessment. *Journal of Advances in Modeling Earth Systems* **2** (2010).

29. C. Jalihal, J. H. C. Bosmans, J. Srinivasan, A. Chakraborty, The response of tropical precipitation to Earth's precession: the role of energy fluxes and vertical stability. *Clim. Past* **15**, 449–462 (2019).

30. W. M. Lewis Jr, Tropical lakes: how latitude makes a difference. *Perspectives in tropical limnology* **4364** (1996).

31. J. E. Tierney, *et al.*, Glacial cooling and climate sensitivity revisited. *Nature* **584**, 569–573 (2020).

32. S. C. Porter, Snowline depression in the tropics during the Last Glaciation. *Quaternary Science Reviews* **20**, 1067–1091 (2000).

33. Y. Garcin, *et al.*, Reconstructing C 3 and C 4 vegetation cover using n -alkane carbon isotope ratios in recent lake sediments from Cameroon, Western Central Africa. *Geochimica et Cosmochimica Acta* **142**, 482–500 (2014).

34. J. R. Ehleringer, T. E. Cerling, B. R. Helliker, C4 photosynthesis, atmospheric CO2, and climate. *Oecologia* **112**, 285–299 (1997).

35. G. J. Collatz, J. A. Berry, J. S. Clark, Effects of climate and atmospheric CO 2 partial pressure on the global distribution of C 4 grasses: present, past, and future. *Oecologia* **114**, 441–454 (1998).

36. T. E. Cerling, J. R. Ehleringer, J. M. Harris, Carbon dioxide starvation, the development of C4 ecosystems, and mammalian evolution. *Phil. Trans. R. Soc. Lond. B* **353**, 159–171 (1998).

37. J. S. Sinninghe Damsté, *et al.*, A 25,000-year record of climate-induced changes in lowland vegetation of eastern equatorial Africa revealed by the stable carbon-isotopic composition of fossil plant leaf waxes. *Earth and Planetary Science Letters* **302**, 236–246 (2011).

38. F. A. Street-Perrott, Impact of Lower Atmospheric Carbon Dioxide on Tropical Mountain Ecosystems. *Science* **278**, 1422–1426 (1997).

39. V. J. Hare, E. Loftus, A. Jeffrey, C. B. Ramsey, Atmospheric CO2 effect on stable carbon isotope composition of terrestrial fossil archives. *Nature Communications* **9** (2018).

40. A. F. Diefendorf, E. J. Freimuth, Extracting the most from terrestrial plant-derived n-alkyl lipids and their carbon isotopes from the sedimentary record: A review. *Organic Geochemistry* **103**, 1–21 (2017).

41. J. E. Tierney, P. B. deMenocal, Abrupt Shifts in Horn of Africa Hydroclimate Since the Last Glacial Maximum. *Science* **342**, 843–846 (2013).

42. W. Liu, H. Yang, Multiple controls for the variability of hydrogen isotopic compositions in higher plant *n* -alkanes from modern ecosystems: VARIABILITY OF HYDROGEN ISOTOPIC COMPOSITIONS. *Global Change Biology* **14**, 2166–2177 (2008).

43. Y. V. Wang, *et al.*, What does leaf wax δD from a mixed C3/C4 vegetation region tell us? *Geochimica et Cosmochimica Acta* **111**, 128–139 (2013).

44. T. J. J. Hanebuth, H. K. Voris, Y. Yokoyama, Y. Saito, J. Okuno, Formation and fate of sedimentary depocentres on Southeast Asia's Sunda Shelf over the past sea-level cycle and biogeographic implications. *Earth-Science Reviews* **104**, 92–110 (2011).

45. B. P. Murphy, D. M. J. S. Bowman, Seasonal water availability predicts the relative abundance of C_3 and C_4 grasses in Australia. *Global Ecol Biogeography* **16**, 160–169 (2007).

46. J. M. Russell, *et al.*, Glacial forcing of central Indonesian hydroclimate since 60,000 y B.P. *Proceedings of the National Academy of Sciences* **111**, 5100–5105 (2014).

47. P. M. J. Douglas, M. Pagani, M. Brenner, D. A. Hodell, J. H. Curtis, Aridity and vegetation composition are important determinants of leaf-wax δD values in southeastern Mexico and Central America. *Geochimica et Cosmochimica Acta* **97**, 24–45 (2012).

48. X. Yuan, M. R. Kaplan, M. A. Cane, The Interconnected Global Climate System—A Review of Tropical–Polar Teleconnections. *J. Climate* **31**, 5765–5792 (2018).

49. A. C. Clement, R. Seager, M. A. Cane, Orbital controls on the El Niño/Southern Oscillation and the tropical climate. *Paleoceanography* **14**, 441–456 (1999).

50. J. Laskar, *et al.*, A long-term numerical solution for the insolation quantities of the Earth. *A&A* **428**, 261–285 (2004).

51. S. Chen, *et al.*, A high-resolution speleothem record of western equatorial Pacific rainfall: Implications for Holocene ENSO evolution. *Earth and Planetary Science Letters* **442**, 61–71 (2016).

52. B. Konecky, J. Russell, S. Bijaksana, Glacial aridity in central Indonesia coeval with intensified monsoon circulation. *Earth and Planetary Science Letters* **437**, 15–24 (2016).

53. J. B. Wurtzel, *et al.*, Tropical Indo-Pacific hydroclimate response to North Atlantic forcing during the last deglaciation as recorded by a speleothem from Sumatra, Indonesia. *Earth and Planetary Science Letters* **492**, 264–278 (2018).

54. H. Cheng, *et al.*, The Asian monsoon over the past 640,000 years and ice age terminations. *Nature* **534**, 640–646 (2016).

55. Zhang, *et al.*, The Asian Summer Monsoon: Teleconnections and Forcing Mechanisms—A Review from Chinese Speleothem δ18O Records. *Quaternary* **2**, 26 (2019).

56. X. Yang, *et al.*, Holocene stalagmite $\delta^{18}O$ records in the East Asian monsoon region and their correlation with those in the Indian monsoon region. *The Holocene* **24**, 1657–1664 (2014).

57. F. S. R. Pausata, D. S. Battisti, K. H. Nisancioglu, C. M. Bitz, Chinese stalagmite δ18O controlled by changes in the Indian monsoon during a simulated Heinrich event. *Nature Geosci* **4**, 474–480 (2011).

58. G. Kathayat, *et al.*, Evaluating the timing and structure of the 4.2 ka event in the Indian summer monsoon domain from an annually resolved speleothem record from Northeast India. *Climate of the Past* **14**, 1869–1879 (2018).

59. H. Dang, *et al.*, Pacific warm pool subsurface heat sequestration modulated Walker circulation and ENSO activity during the Holocene. *Sci. Adv.* **6**, eabc0402 (2020).

60. S. Chawchai, *et al.*, Hydroclimatic shifts in northeast Thailand during the last two millennia – the record of Lake Pa Kho. *Quaternary Science Reviews* **111**, 62–71 (2015).

61. M. Blaauw, J. A. Christen, Flexible paleoclimate age-depth models using an autoregressive gamma process. *Bayesian Anal.* **6**, 457–474 (2011).

62. P. J. Reimer, *et al.*, IntCal13 and Marine13 Radiocarbon Age Calibration Curves 0–50,000 Years cal BP. *Radiocarbon* **55**, 1869–1887 (2013).

63. C. Waelbroeck, *et al.*, Sea-level and deep water temperature changes derived from benthic foraminifera isotopic records. *Quaternary Science Reviews* **21**, 295–305 (2002).

64. J. E. Rattray, R. H. Smittenberg, Separation of Branched and Isoprenoid Glycerol Dialkyl Glycerol Tetraether (GDGT) Isomers in Peat Soils and Marine Sediments Using Reverse Phase Chromatography. *Front. Mar. Sci.* **7** (2020).

65. J. W. H. Weijers, S. Schouten, J. C. van den Donker, E. C. Hopmans, J. S. Sinninghe Damsté, Environmental controls on bacterial tetraether membrane lipid distribution in soils. *Geochimica et Cosmochimica Acta* **71**, 703–713 (2007).

66. E. C. Hopmans, S. Schouten, J. S. Sinninghe Damsté, The effect of improved chromatography on GDGT-based palaeoproxies. *Organic Geochemistry* **93**, 1–6 (2016).

67. C. Zhu, *et al.*, Comprehensive glycerol ether lipid fingerprints through a novel reversed phase liquid chromatography–mass spectrometry protocol. *Organic Geochemistry* **65**, 53–62 (2013).

68. C. De Jonge, *et al.*, Occurrence and abundance of 6-methyl branched glycerol dialkyl glycerol tetraethers in soils: Implications for palaeoclimate reconstruction. *Geochimica et Cosmochimica Acta* **141**, 97–112 (2014).

69. B. D. A. Naafs, *et al.*, Introducing global peat-specific temperature and pH calibrations based on brGDGT bacterial lipids. *Geochimica et Cosmochimica Acta* **208**, 285–301 (2017).

70. I. Harris, P. D. Jones, T. J. Osborn, D. H. Lister, Updated high-resolution grids of monthly climatic observations – the CRU TS3.10 Dataset. *International Journal of Climatology* **34**, 623–642 (2014).

71. I. Harris, T. J. Osborn, P. Jones, D. Lister, Version 4 of the CRU TS monthly high-resolution gridded multivariate climate dataset. *Scientific Data* **7**, 1–18 (2020).

72. E. Monnin, EPICA Dome C high resolution carbon dioxide concentrations (2006) https:/doi.org/10.1594/PANGAEA.472488 (January 6, 2021).

73. K. K. Andersen, *et al.*, High-resolution record of Northern Hemisphere climate extending into the last interglacial period. *Nature* **431**, 147–151 (2004).

74. B. D. A. Naafs, A. V. Gallego-Sala, G. N. Inglis, R. D. Pancost, Refining the global branched glycerol dialkyl glycerol tetraether (brGDGT) soil temperature calibration. *Organic Geochemistry* **106**, 48–56 (2017).

75. D. R. Legates, C. J. Willmott, Mean seasonal and spatial variability in gauge-corrected, global precipitation. *International Journal of Climatology* **10**, 111–127 (1990).

76. R. W. Spencer, Global Oceanic Precipitation from the MSU during 1979—91 and Comparisons to Other Climatologies. *Journal of Climate* **6**, 1301–1326 (1993).

77. T.C. Peterson T.C. and R.S. Vose X. Global Historical Climatology Network - Monthly (GHCN-M), Version 2. NOAA National Centers for Environmental Information. (1997) doi:10.7289/V5X34VDR [accessed 15 October 2020 using http://climexp.knmi.nl]

Acknowledgments

We wish to thank Sherilyn Fritz, Wichuratree Klubseang and Sudo Inthonkaew for sampling assistance and discussion. Jayne Rattray and Anna Hägglund and Camilla Bredberg are thanked for laboratory assistance. Paula Reimer from Queen's University of Belfast conducted the radiocarbon analyses.

Funding This work was supported by Swedish Research Council (VR) research grants 621-2008-2855 (RHS), 348-2008-6071 (BW) and 621-2011-4916 (BW).

Author contributions

Conceptualization: BW, RHS
Sampling: BW, KAY, AC, SC
Analysis: BW, KAY, RHS, MV, SC
Supervision: RHS, BW
Writing—original draft: RHS
Writing—review & editing: RHS, BW, KYA, FS, MV, SC, AC

Competing interests: Authors declare that they have no competing interests.

Data and materials availability: The data presented in this paper is available online as csv files and as excel file at the Bolin Centre of Climate Research Database: (link).

Figures

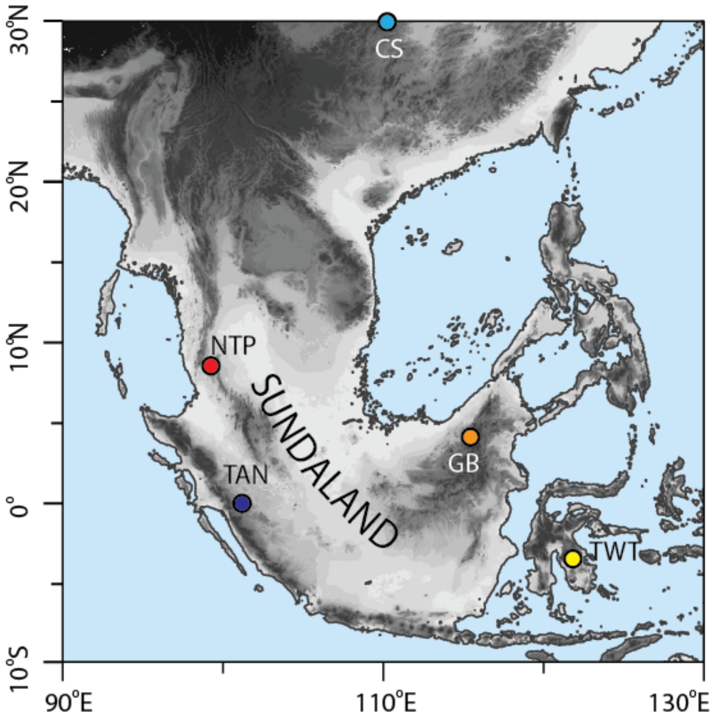

Fig. 1. Location of Lake Nong Thale Prong (NTP) and other records mentioned in the text. GB: Gunung Buda National Park speleothem, Borneo; TWT: Lake Towuti, Sulawesi; CS: Chinese Speleothems; TAN: Tangga cave, Sumatra. The map shows the extent of the emerged landscapes of former Sundaland during the last glacial maximum sea level low stand.

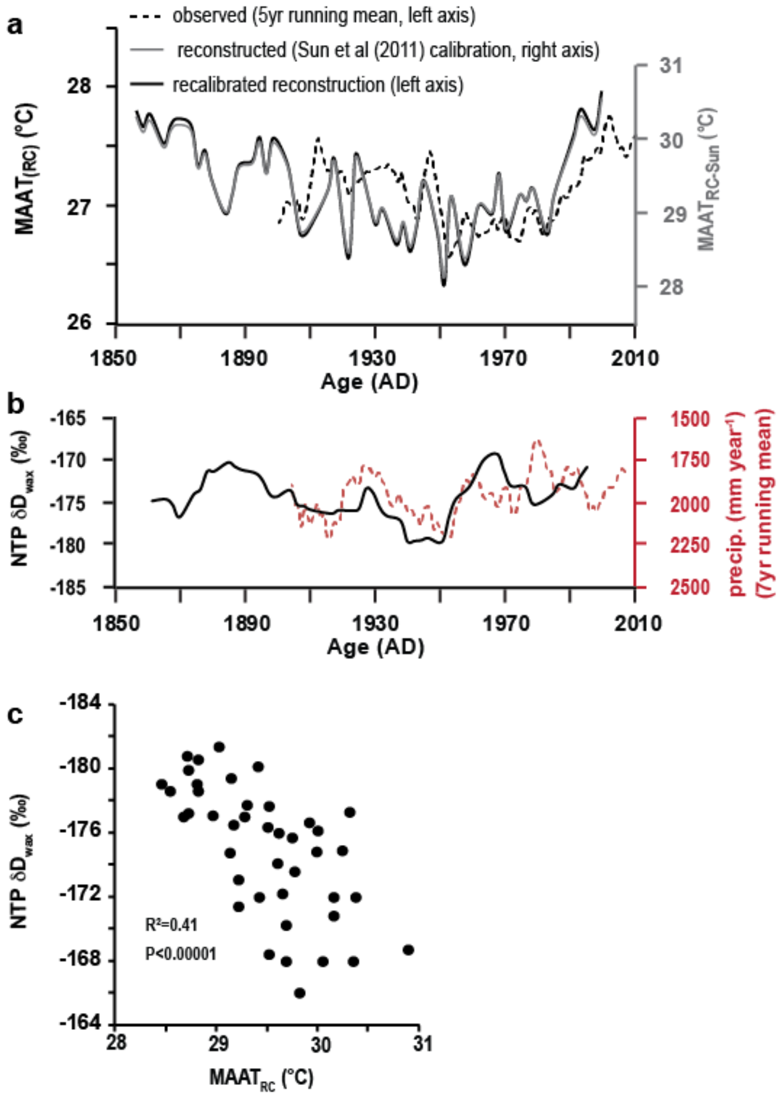

Fig. 2. Comparison of instrumental climate data with proxy data measured on the NTP surface sediments. a) Mean Annual Air Temperature ($MAAT_{RC\text{-}Sun}$) reconstructed using bacterial-derived branched GDGTs (right axis, grey), compared to observations (left axis, stippled black). To obtain a local calibration the reconstructed MAAT was scaled for amplitude and mean (see SI) to correspond with the instrumental record (black, left axis). b) Instrumental rainfall data (right axis, stippled red) compared with δD_{wax} data from the same samples (17) suggests a good correlation between the two. c) Scatter plot of dD_{wax} and reconstructed MAAT from the same samples. Instrumental climate data are taken from the CRU TS monthly high-resolution gridded multivariate climate dataset, Version 4 (71).

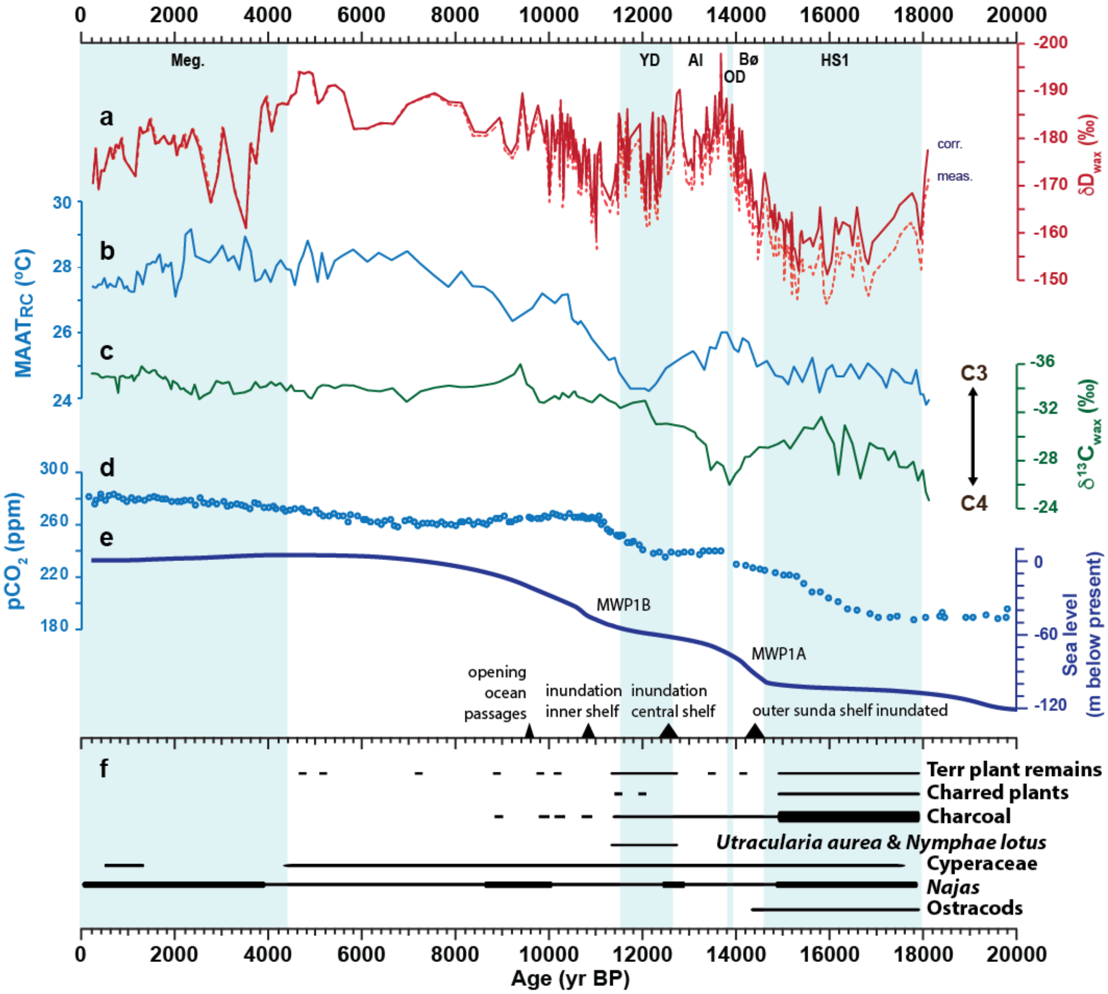

Fig. 3. Proxy records of lake NTP of the last 18,000 years. a) dD$_{wax}$, both as measured and corrected (stippled) for global sea level change. **b**) Reconstructed mean annual air temperature (MAAT$_{RC}$). **c**) d^{13}C$_{wax}$. **d**) Atmospheric CO_2 levels (72). **e**) Sea level reconstruction for the Sunda Shelf region (44) **f**) Macrofossil and charcoal results. Thick line: very abundant; Thin line: present.
Meg: Meghalayan period; YD: Younger Dryas; Al: Allerød; OD: Older Dryas; Bø:Bølling; HS1: Heinrich Stadial 1. MWP: Meltwater pulses.

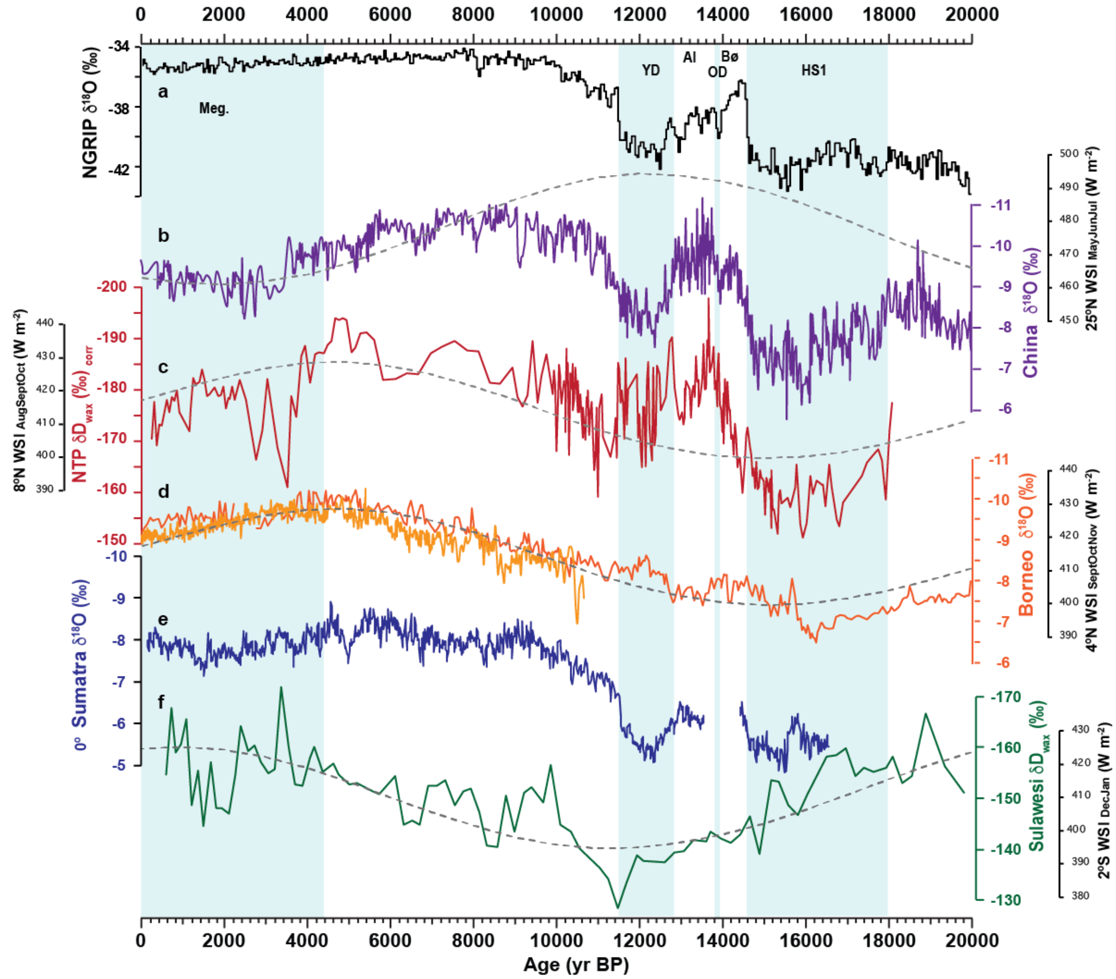

Fig. 4. Comparison of isotope records. **a**) Greenland ice core d^{18}O as a reference for NH temperature (73). **b**) Combined Chinese speleothem d^{18}O (54). **c**) NTP dD$_{wax}$ corrected for sea level effect (this study). **d**) Borneo speleothem d^{18}O record (dark(12) and light (51) orange). **e**) Sumatra speleothem d^{18}O record (53). **f**) Sulawesi dD$_{wax}$ record (52). b-f are all plotted on the same scale where one unit in d ^{18}O corresponds to 8 units in d D space, according to the global meteoric water line. Grey dotted lines over b-d and f show the solar irradiation averaged for the 2 or 3 wettest months (WSI: Wet Season Insolation) for the latitudes of the respective records (50). No clear wettest period could be defined for Sumatra (see SI). Time periods are shown as in in Figure 3.

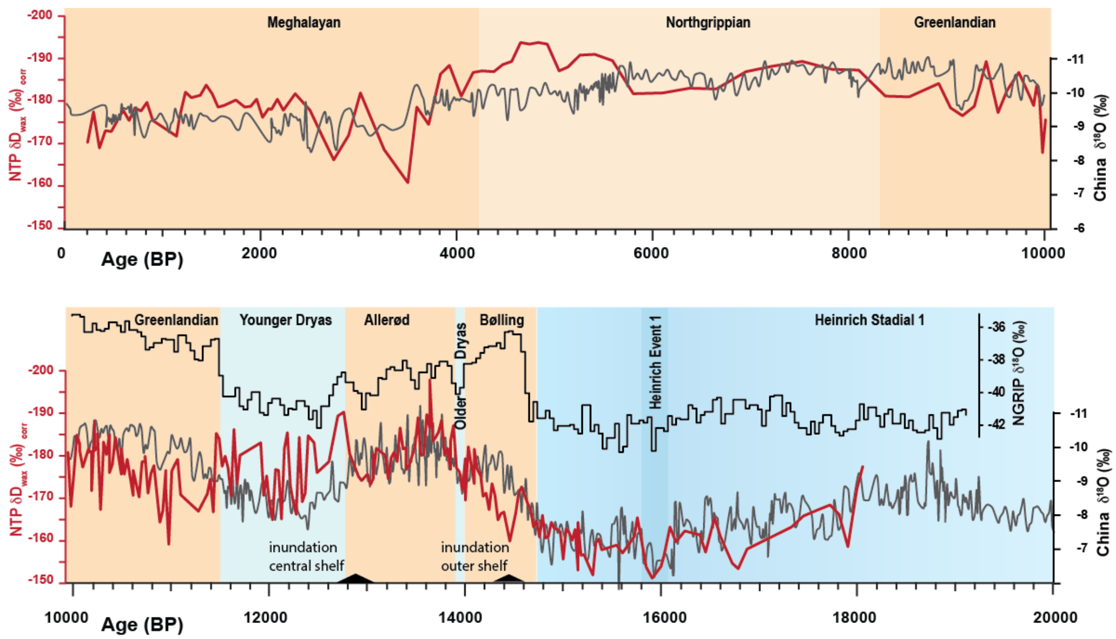

Fig. 5. Comparison of the NTP δD_{wax} (this study) with the Chinese speleothem δ^{18}O records (54). Both records resemble each other very well, including a number of short-term events like Heinrich Event 1. For reference, the deglacial Greenland δ^{18}O (73) record is also plotted. The records are scaled in the same way as in Fig. 4.

Supplementary Materials

Figures S1-S10

Tables S1-S8 (as excel file), are also available at the Bolin Center for Climate Research database: (link will be provided)

Science Advances

AAAS

Supplementary Materials for

A 18,000-year Record of Tropical Land Temperature, Convective Activity and Rainfall Seasonality from The Maritime Continent

Rienk H Smittenberg *, Kweku A Yamoah, Frederik Schenk, Akkaneewut Chabangborn, Sakonvan Chawchai, Minna Väliranta, Barbara Wohlfarth*

*Corresponding authors. Email: rienk.smittenberg@geo.su.se; barbara.wohlfarth@geo.su.se

This PDF file includes:

Figures S1 to S10

Other Supplementary Materials for this manuscript include the following:

Table 1. Composite stratigraphy
Table 2. Radiocarbon Data
Table 3. Plant macrofossil and charcoal data
Table 4. Bulk geochemistry: TOC, TN, LOI, δ^{13}Cbulk and $\delta^{15}N_{bulk}$
Table 5. Leaf wax δD
Table 6. Leaf wax δ^{13}C
Table 7. GDGTs and reconstructed MAAT
Table 8. Surface Core GDGTs, reconstructed MAAT, leaf wax δD and instrumental MAAT

Supplementary figures

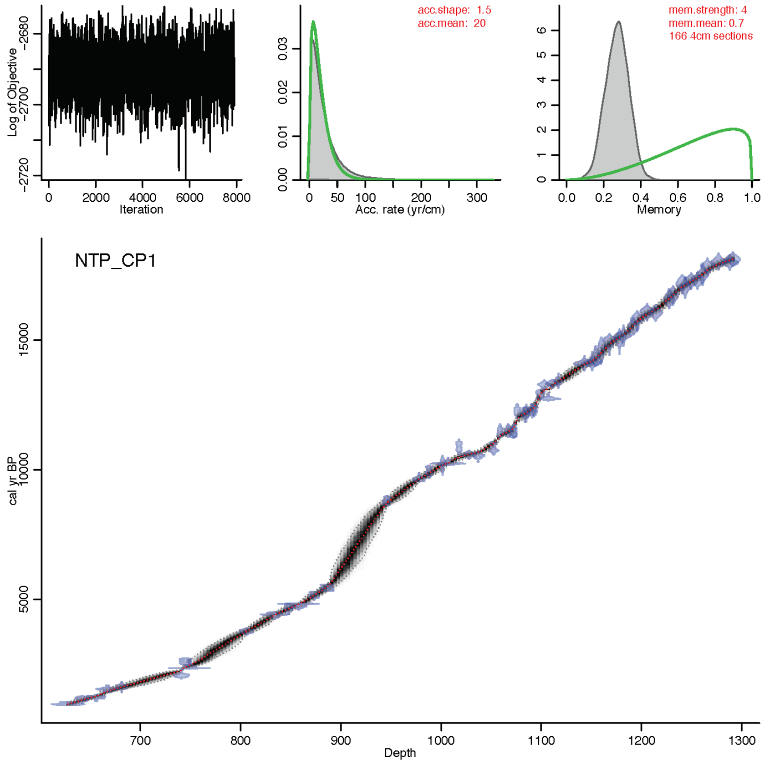

Figure S1. Age model of Lake Nong Thale Prong. Depth is expressed in meter below lake level.

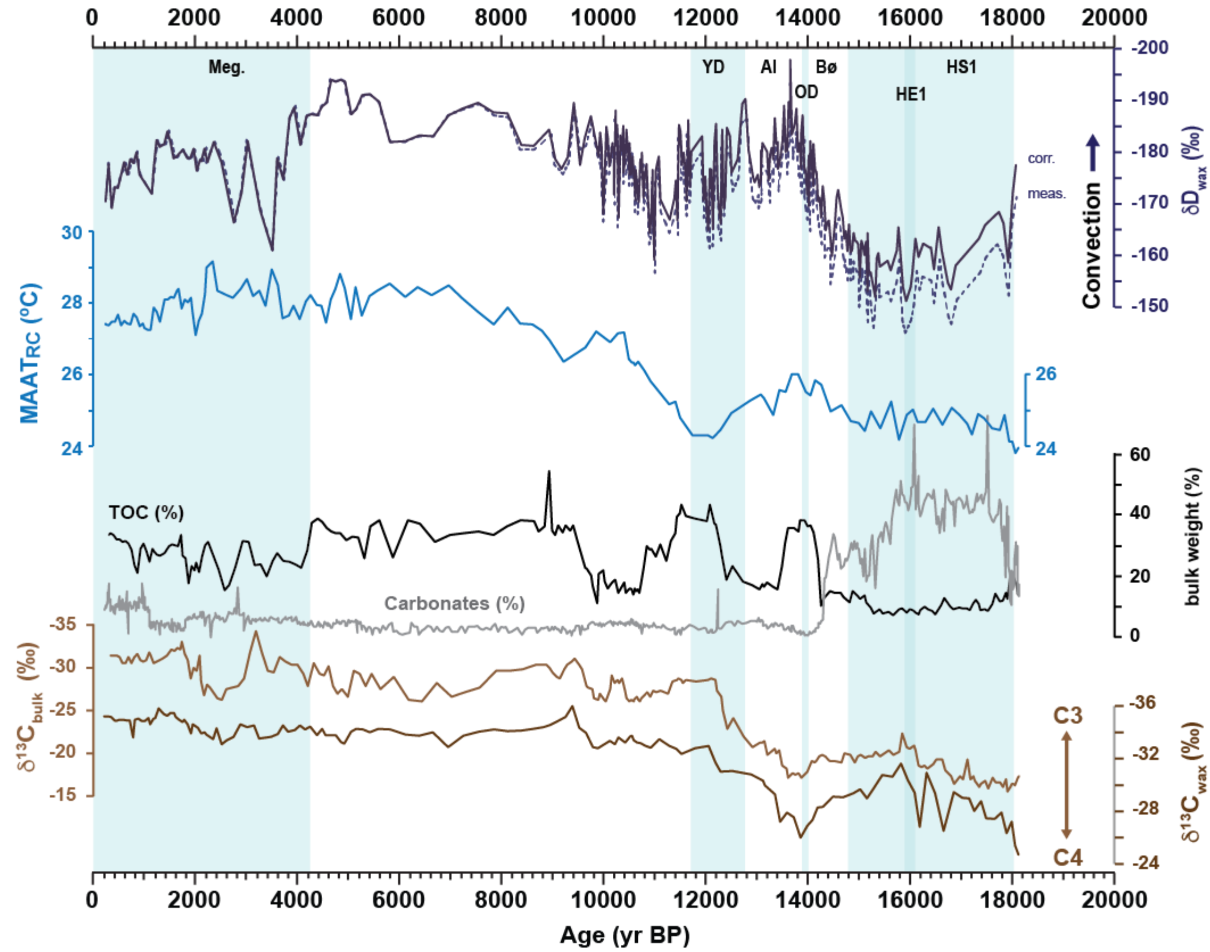

Figure S2. Proxy records of lake Nong Thale Prong, with elements of Fig. 3 in the main paper, extended with TOC content, bulk $\delta^{13}C$, and carbonate content based on loss-on-ignition.

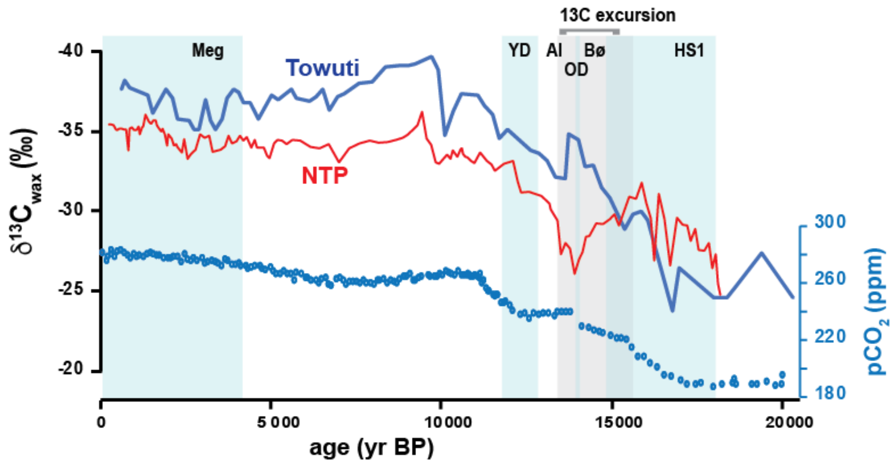

Figure S3. Comparison of the $\delta^{13}C_{wax}$ records of lake NTP (this study) and lake Towuti (46) and atmospheric CO_2 levels (72).

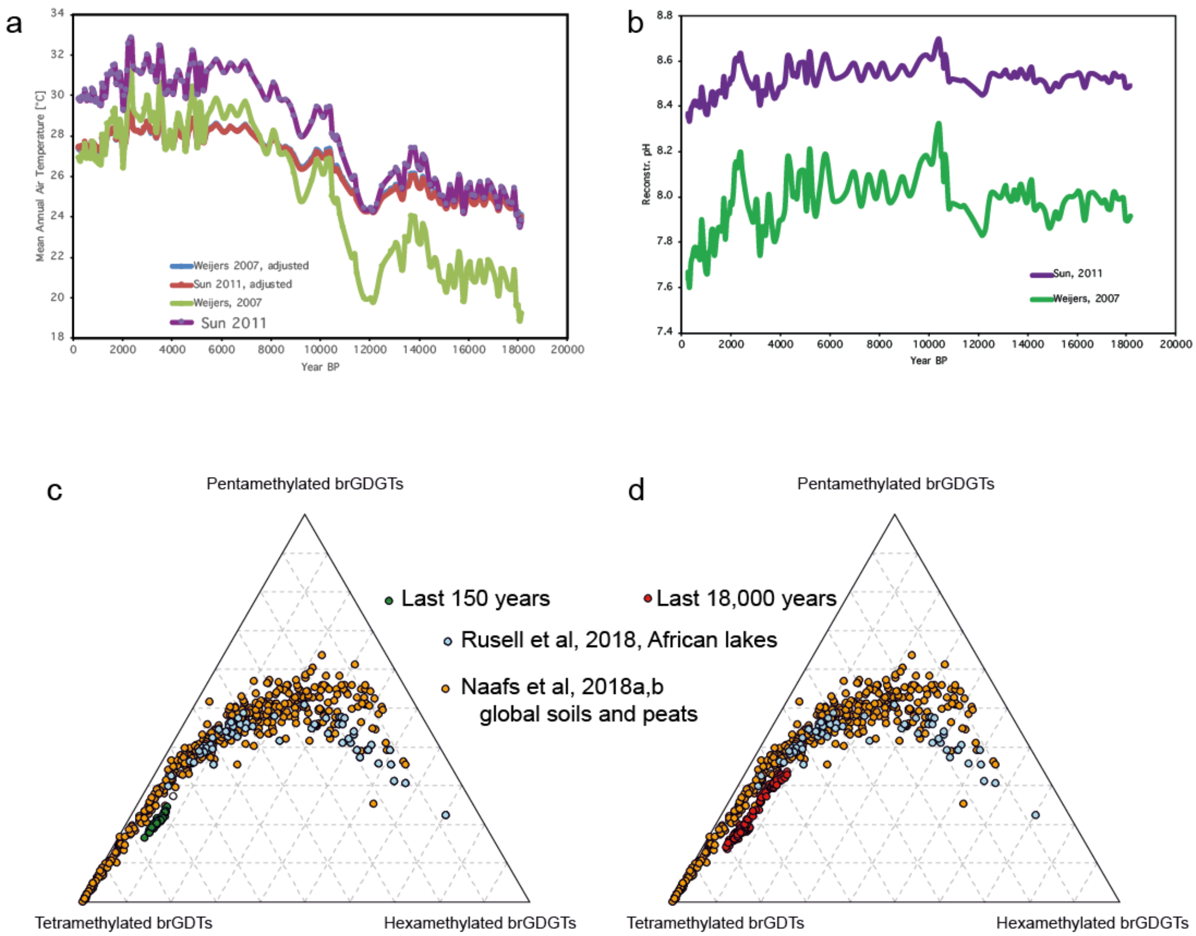

Figure S4. a) Reconstructed MAAT using the MBT/CBT ratios according to two calibrations (22,65), and after local recalibration as described in the text. b) reconstructed pH using the CBT ratios (3)(4), c) Triplot of the relative abundance of tetra, penta- and hexamethylated GDGTs in the surface core (green); a the pooled soil and peat (69,74) (orange) and an African lake dataset (7)(light blue) are plotted for reference. d) the same as c, but for the long core NTP data (in red). The reference data set includes both the 5- and 6-methyl GDGTs, while the NTP dataset includes all isomers of the same *m/z*.

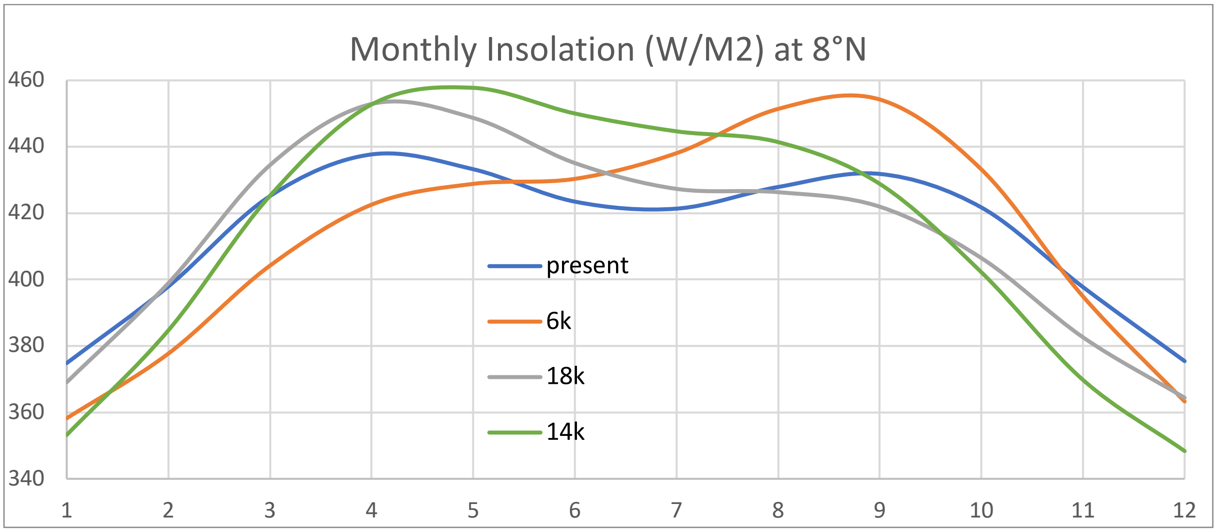

Figure S5. Annual insolation curves at 8°N over selected periods from the last 18,000 years (20) clearly showing the two maximums in April and August/September regardless of time period. Months are in numbers.

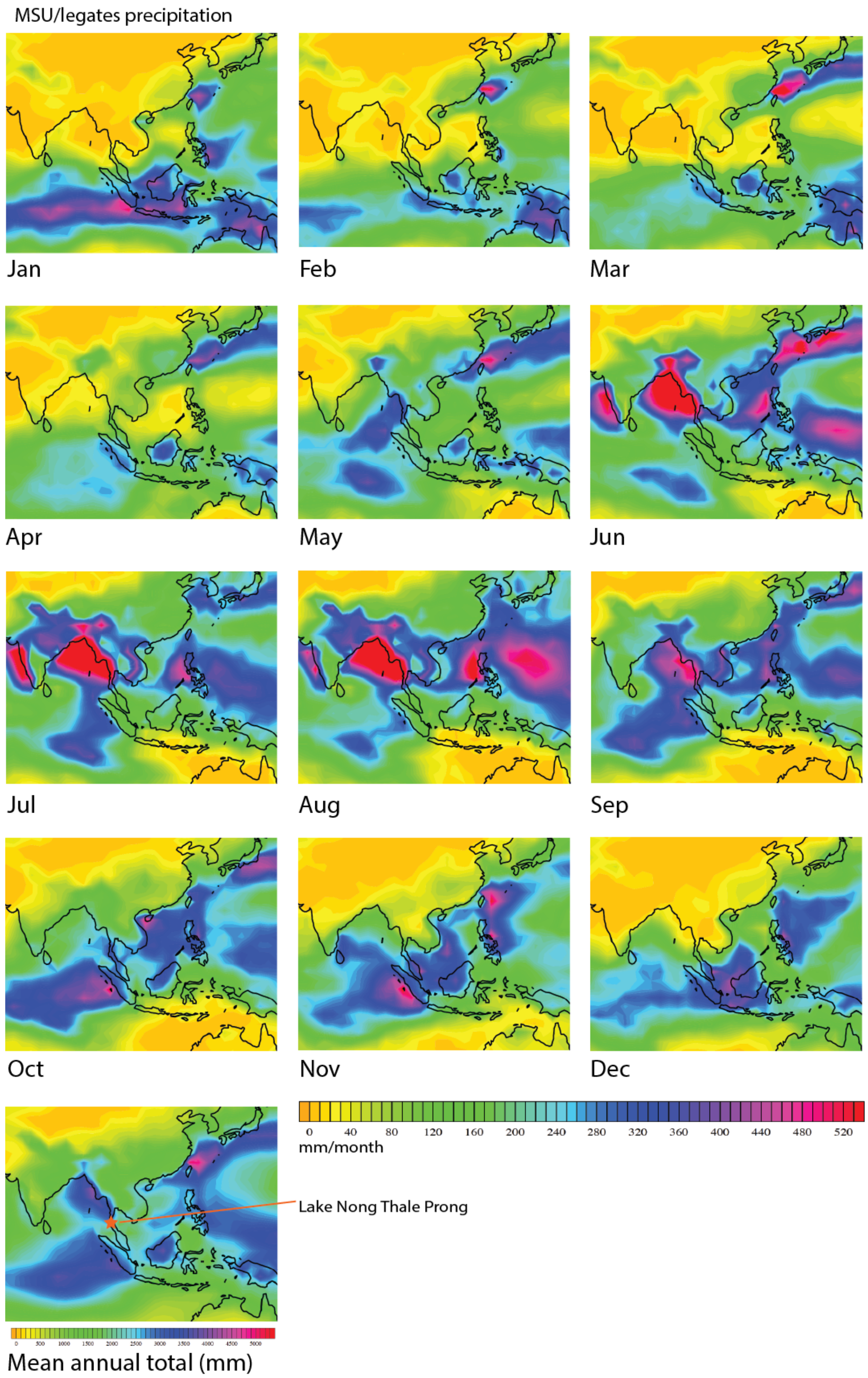

Figure S6. Monthly precipitation of the maritime continent and SE Asia. The wettest months at Lake Nong Thale Prong are associated with the southward passing of the ITCZ from September to November. Maps from http://research.jisao.washington.edu/legates_msu/#analyses (75,76).

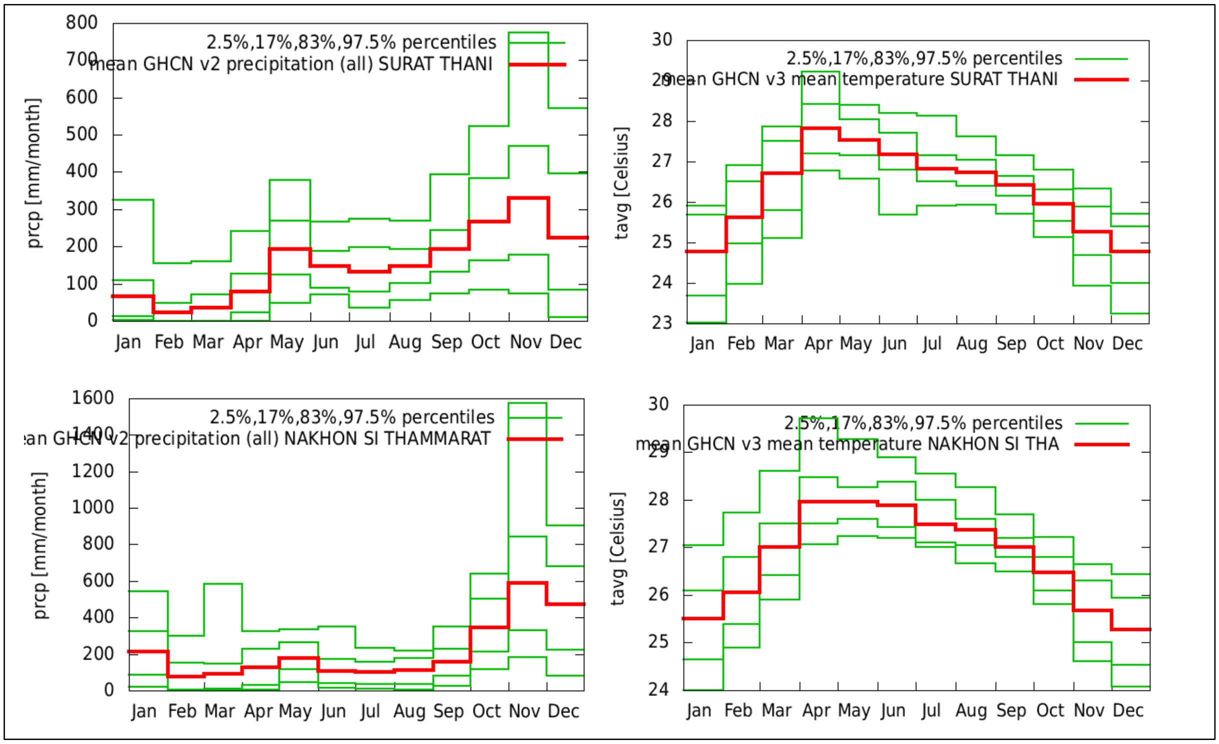

Figure S7. Monthly meteorological data from the two nearest weather stations to lake NTP, Surat Thani (9.12N, 99.35E) and Nakhon Si Thammarat (8.47N, 99.97E), obtained from the Global Historical Climatology Network (GHCN-Monthly) database Version 2. (77)
The wettest period is September-November, running even into December (left panels); the warmest months are April-May.

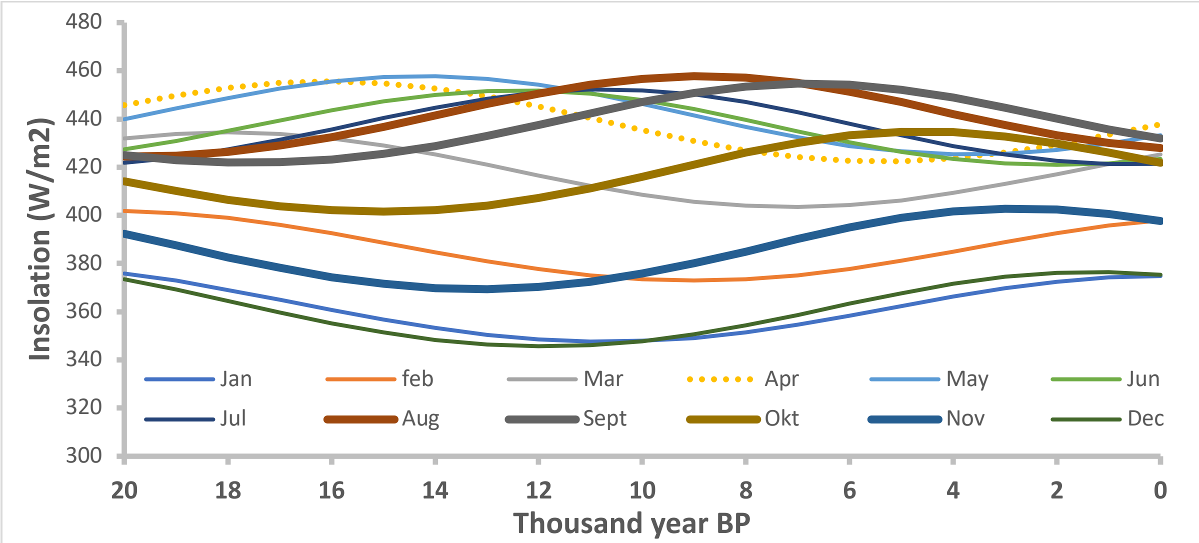

Figure S8. Mean monthly insolation (W/m^2) over the last 20,000 years for 8°N (50), showing the waxing and waning of insolation energy over the precessional cycle for the various months. Insolation maximizes between 6-4 kyr BP for the wettest period SON (See Fig. S7). The insolation curves have the same shape for higher latitudes, but have different absolute values. The mainland SE Asian summer monsoon peaks in JAS, with highest insolation between 10-8 kyr BP and very low insolation at the present. Note that the age axis is reverse compared to proxy records.

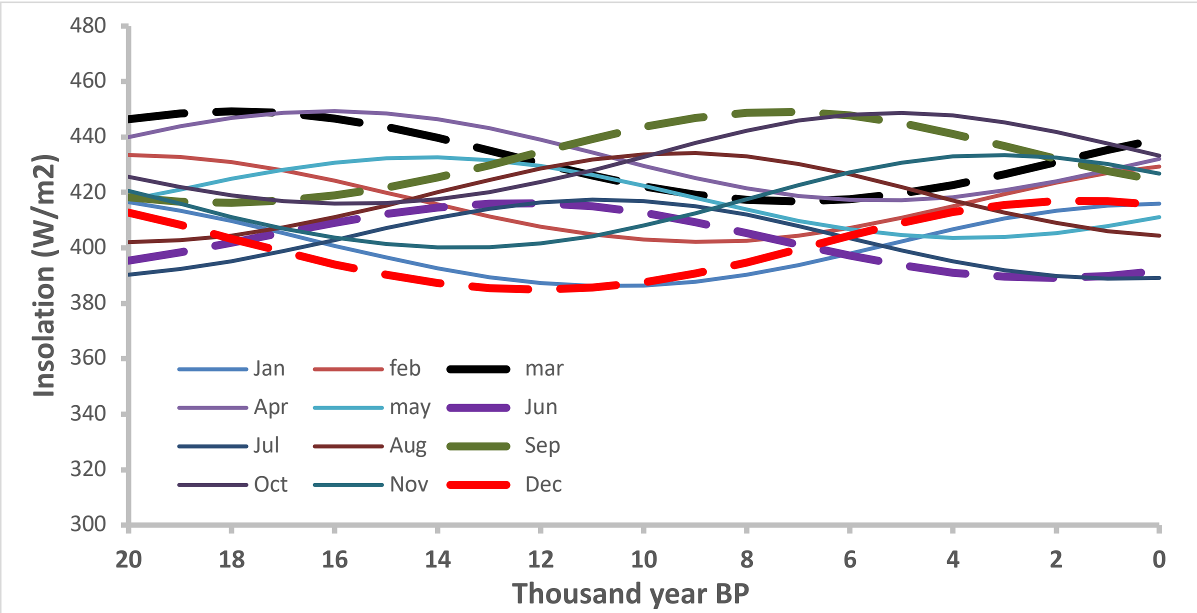

Figure S9. As Figure S8 but for 0° (equator). Present-day June and July insolation are at their precessional low, and these months have correspondingly lowest rainfall amounts (see (53), while the months of December and January, with the same angle of the sun, have stronger insolation and greater rainfall (See Fig S10). Assuming a dominant influence of insolation on convective activity, the annual precipitation patterns likely changes over the course of the precessional cycle.

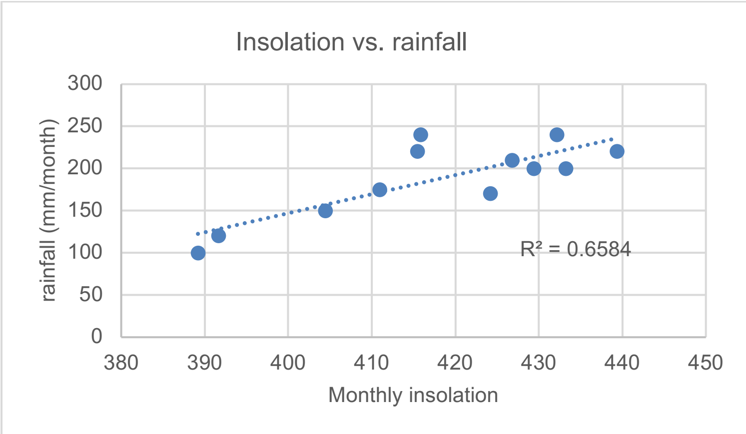

Figure S10. Cross plot of monthly rainfall against monthly insolation for 0° (equator), showing a clear correlation between the two. Rainfall data taken from (53) and insolation for the present day (0 ka BP) of Fig. S9.

References

numbering as in main text

20. J. M. Russell, E. C. Hopmans, S. E. Loomis, J. Liang, J. S. S. Damsté, Distributions of 5- and 6-methyl branched glycerol dialkyl glycerol tetraethers (brGDGTs) in East African lake sediment: Effects of temperature, pH, and new lacustrine paleotemperature calibrations. *Organic Geochemistry* **117**, 56–69 (2018).

22. Q. Sun, *et al.*, Distributions and temperature dependence of branched glycerol dialkyl glycerol tetraethers in recent lacustrine sediments from China and Nepal. *Journal of Geophysical Research: Biogeosciences* **116** (2011).

46. J. M. Russell, *et al.*, Glacial forcing of central Indonesian hydroclimate since 60,000 y B.P. *Proceedings of the National Academy of Sciences* **111**, 5100–5105 (2014).

50. J. Laskar, *et al.*, A long-term numerical solution for the insolation quantities of the Earth. *A&A* **428**, 261–285 (2004).

53. J. B. Wurtzel, *et al.*, Tropical Indo-Pacific hydroclimate response to North Atlantic forcing during the last deglaciation as recorded by a speleothem from Sumatra, Indonesia. *Earth and Planetary Science Letters* **492**, 264–278 (2018).

65. J. W. H. Weijers, S. Schouten, J. C. van den Donker, E. C. Hopmans, J. S. Sinninghe Damsté, Environmental controls on bacterial tetraether membrane lipid distribution in soils. *Geochimica et Cosmochimica Acta* **71**, 703–713 (2007).

69. B. D. A. Naafs, *et al.*, Introducing global peat-specific temperature and pH calibrations based on brGDGT bacterial lipids. *Geochimica et Cosmochimica Acta* **208**, 285–301 (2017).

72. E. Monnin, EPICA Dome C high resolution carbon dioxide concentrations (2006) https:/doi.org/10.1594/PANGAEA.472488 (January 6, 2021).

74. B. D. A. Naafs, A. V. Gallego-Sala, G. N. Inglis, R. D. Pancost, Refining the global branched glycerol dialkyl glycerol tetraether (brGDGT) soil temperature calibration. *Organic Geochemistry* **106**, 48–56 (2017).

75. D. R. Legates, C. J. Willmott, Mean seasonal and spatial variability in gauge-corrected, global precipitation. *International Journal of Climatology* **10**, 111–127 (1990).

76. R. W. Spencer, Global Oceanic Precipitation from the MSU during 1979—91 and Comparisons to Other Climatologies. *Journal of Climate* **6**, 1301–1326 (1993).

77. T. C. Peterson and R. S. Vose. Global Historical Climatology Network - Monthly (GHCN-M), Version 2. NOAA National Centers for Environmental Information (1997): doi:10.7289/V5X34VDR [accessed 15 October 2020 using http://climexp.knmi.nl]